Electroexcitation of low-multipolarity magnetic transitions in ^{36}Ar and ^{38}Ar

C. W. Foltz,* D. I. Sober, and L. W. Fagg
Catholic University of America, Washington, D.C. 20064

H. D. Gräf, A. Richter, and E. Spamer
Institut für Kernphysik, Technische Hochschule Darmstadt, 6100 Darmstadt, Germany

B. Alex Brown
National Superconducting Cyclotron Laboratory and Department of Physics and Astronomy, Michigan State University, East Lansing, Michigan 48824

(Received 26 January 1993)

Measurements of inelastic electron scattering from ^{36}Ar and ^{38}Ar have been performed at low energy and backward angle to determine the distribution of $M1$ and $M2$ strength in these nuclei. The total observed $M1$ strength in ^{36}Ar is approximately 93% of that predicted in the measured energy region by shell-model calculations using effective $M1$ operators. In ^{38}Ar, the single strong $M1$ transition predicted by shell-model calculations was not observed. Instead, a number of weak transitions were observed, with total $M1$ strength equal to about 134% of the predicted strength.

PACS number(s): 25.30.Dh, 27.30.+t

I. INTRODUCTION

The strong concentration of ΔT=1 magnetic dipole ($M1$) transition strength among the self-conjugate nuclei of the lower $1s0d$ shell has been extensively studied by electron scattering [1–4] and by resonance fluorescence [5–7] techniques. For the self-conjugate nuclei in the upper part of the shell, i.e., ^{32}S and ^{36}Ar, the $M1$ strength appears to be more fragmented, [8,9] although the fragmentation was not well determined in these earlier experiments due to limited resolution.

We report here on measurements of backward-angle electron scattering from ^{36}Ar and ^{38}Ar. The energy resolution of the new experiment is considerably higher than that of previous measurements on ^{36}Ar [9], while ^{38}Ar has not been studied before by electron scattering. The $A = 4N+2$ nuclei in the upper $1s0d$ shell have in general been even less studied than their self-conjugate neighbors, and the systematics of such nuclei are only beginning to emerge.

The measurements on ^{36}Ar and ^{38}Ar were performed at large scattering angles, 153° and 117°, in order to enhance magnetic transitions relative to electric transitions. Cross sections were measured at low momentum transfers, $0.25 < q < 0.55$ fm^{-1}, so that $M1$ and $M2$ transitions would be strongly enhanced relative to all higher-multipolarity transitions.

In addition to the intrinsic interest in the magnitude and distribution of the $M1$ and $M2$ transition strengths in these two nuclei, the principal motivation for this experiment arises from the general interest in the apparent quenching of such strength in these and heavier nuclei. Since the $1s0d$ shell is the highest for which complete shell-model calculations have been made [10], the behavior of the magnetic strength in nuclei of the upper $1s0d$ shell may serve as a useful reference from which to extrapolate such behavior in the heavier nuclei. Shell-model calculations that include higher-order configuration mixing can largely account for the observed $M1$ strength, at least in many light nuclei ($A \leq 40$) [7]. The quenching which arises from meson exchange and Δ-isobar effects is expected to be less significant [10–13]. In any case, it is evident that a more accurate determination of the strength and location of $M1$ transitions throughout a range of nuclides is needed to further test these quenching theories.

In Sec. II we describe the apparatus and experimental techniques used in the measurements. The extraction of cross sections and identification of transition multipolarities and strengths are discussed in Secs. III and IV. The experimental results are interpreted in light of current shell-model calculations and sum rules in Secs. V and VI. We give some conclusions in Sec. VII. More details of all aspects of the experiment, analysis, and results can be found in Ref. [14].

II. EXPERIMENTAL TECHNIQUES

Isotopically enriched gas targets of ^{36}Ar (98.6%) and ^{38}Ar (96.2%) were exposed to the electron beam of the Darmstadt Linear Accelerator (DALINAC) [15]. Data were taken in dispersion-matching mode at six incident energies ranging from 25.5 to 63.0 MeV and at scattering angles of 153° and 117°, with beam currents that averaged about 7 μA.

*Present address: St. Lawrence University, Canton, NY 13617.

The argon gas was contained in a thin-walled cylindrical aluminum target cell, 3 cm in diameter, with its axis vertical (Fig. 1). The target cells were operated at a pressure of about 550 kPa for ^{36}Ar and about 450 kPa for ^{38}Ar, which gave a total argon thickness of 29 and 24 mg/cm^2, respectively. The cells were similar in design to those used by Bender [16] and Rangacharyulu *et al.* [17], but were made smaller in volume because of the very high cost of the ^{38}Ar gas. The thin portion (90 μm$\approx$ 24 mg/cm^2) of the cell wall was 2.5 cm in height, which easily accommodated the 1.2-cm-high dispersion-matching beam.

To avoid detecting electrons which scattered from the cell walls, a set of front slits [17] was placed between the target cell and the spectrometer entrance slits. The front slit geometry, together with the spectrometer slits, determined both the observed target gas thickness and the solid angle acceptance. The use of the front slits limited the scattering angle in this experiment to a maximum of 153°.

Even with the front slits, some cell-wall-induced events were registered due to rescattering from portions of the cell wall which were in the line of sight of the spectrometer. The empty-cell counting rate was measured to be about 20% of the full-cell rate. Since the empty-target spectrum exhibited no significant peaks, no subtraction was performed. Instead, the empty-target contribution was fitted as part of the smooth background which also included such effects as the elastic radiation tail and ambient radiation.

The target cells were filled with argon using a gas transfer system, shown in Fig. 2, based on that of Ref. [18]. The system consisted of a low-volume manifold with a small-volume reservoir at the end of a 1 m length of stainless steel tubing (1 mm diameter) which could be inserted into a liquid helium dewar. The manifold was connected by valves to the argon gas bottle, the target cell, and a vacuum pump, and was equipped with a pressure sensor. After the manifold and target cell were evacuated, argon was let into the manifold and condensed in the liquid-helium-cooled reservoir. Once the bottle valve had been closed, the tubing was withdrawn from the dewar, and the argon was allowed to expand through the manifold into the target cell. This procedure was repeated until the desired target pressure was reached. Separate cells were filled with ^{36}Ar and ^{38}Ar, and these were alternated with an empty cell during the measurements.

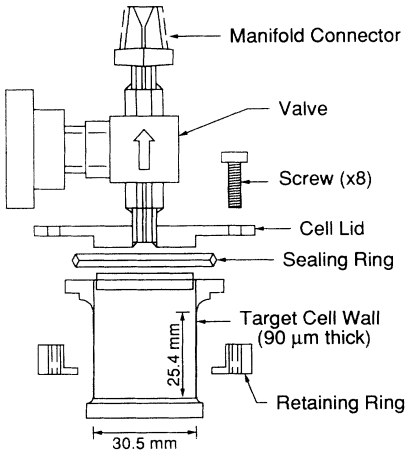

FIG. 1. Construction of gas target cell.

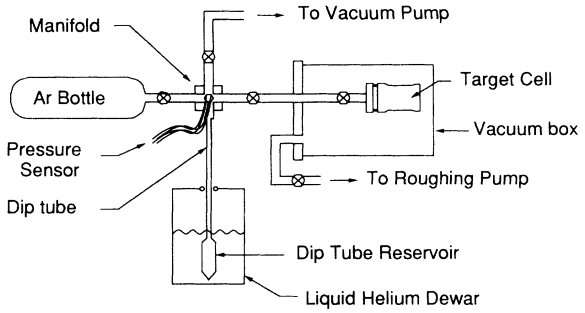

FIG. 2. Gas transfer system used for filling target cells.

Once the target cell was filled and removed from the filling manifold, there was no means to monitor its pressure. Although the temperature and pressure of the gas increased due to electron beam heating, the average density of the gas in the closed cell remained constant. In previous experiments with a similar target cell [16,17] measurements of count rate vs incident beam intensity indicated that the local density changes due to beam heating were less than 1%, so no corrections were applied here. The counting rate from each target with the elastic peak centered in the spectrometer was monitored frequently during the runs to ensure that gas did not leak from the target cells. No statistically significant changes were observed.

The data were taken using the Darmstadt "magic-angle" spectrometer in dispersion-matching mode [19,20]. Although passage of the beam through the cell walls did not contribute directly to the count rate, they did contribute to the energy straggling, and the resulting energy resolution was typically 50 keV FWHM. Although well short of the intrinsic resolving capability of the Darmstadt system, this resolution was nearly a factor of 4 better than that of the previous inelastic electron scattering measurements on ^{36}Ar [9].

For each target gas, electron energy, and spectrometer angle, measurements were made of the elastic peak and of the excitation energy region between approximately 6.5 and 15 MeV. Data were taken by stepping the spectrometer magnetic field and recording the resulting spectra from the 64-channel scintillation counter hodoscope. Four to six days of running time were spent on each target at each energy and angle. These raw spectra were converted to excitation energy spectra by a bin-sorting program, calibrated relative to the corresponding elastic peak. Typical spectra are shown in Figs. 3 and 4.

The E_x spectra were fitted using a peak-fitting code, derived from the program IPA [21], which represented each peak by a modified Gaussian function with its own radiative tail. As earlier experiments with a similar gas

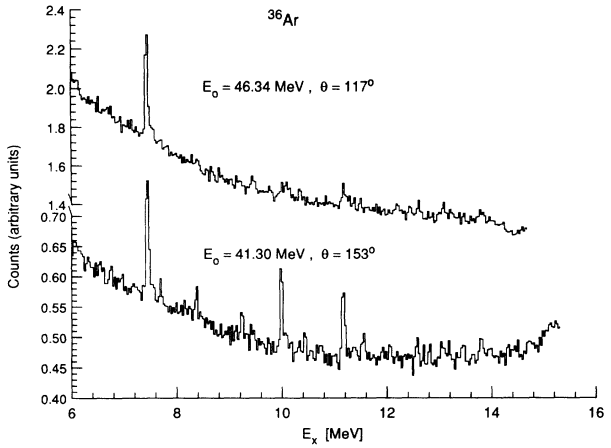

FIG. 3. Excitation energy spectra for ^{36}Ar at momentum transfer $q \approx 0.36$ fm^{-1} and two different scattering angles.

target at Darmstadt [16,17] indicated that the continuous background under the spectra was due predominantly to rescattering from the target cell wall, no attempt was made to calculate a realistic elastic radiative tail. Instead, the background for each spectrum was fitted empirically by a five-parameter polynomial function which was carefully inspected to ensure that it did not introduce any structure which would influence the fitting of narrow peaks. The shape parameters of the inelastic peaks were determined by a fit to the corresponding elastic peak at the same energy and angle, since the elastic peak had better statistics and negligible background. There was no evidence for any variation of width among the inelastic peaks of a run. An example of a fitted spectrum is shown in Fig. 5.

The spectra from each target contained a few strong inelastic peaks which stood out unambiguously above the background, and a much larger number of small possible peaks of dubious statistical significance. After a first analysis of all the spectra, a preliminary list was compiled of all significant peaks which appeared in two or

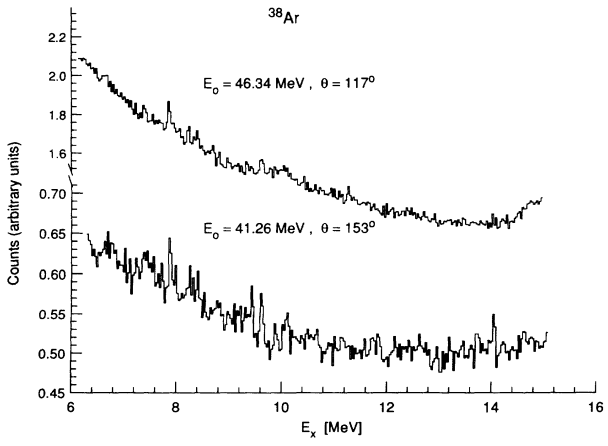

FIG. 4. Excitation energy spectra for ^{38}Ar at momentum transfer $q \approx 0.36$ fm^{-1} and two different scattering angles.

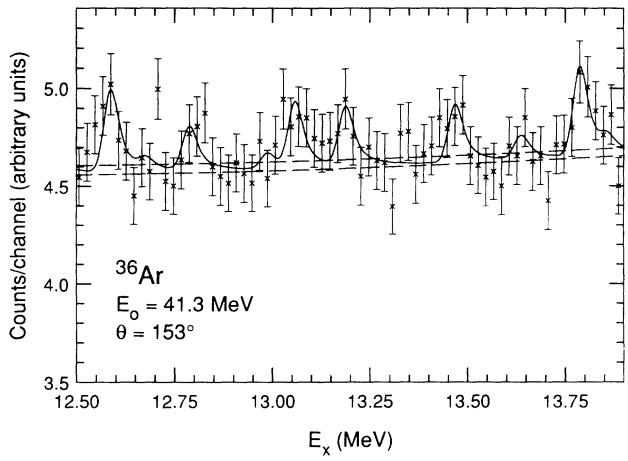

FIG. 5. Example of a fitted spectrum for ^{36}Ar, with alternative (high and low) backgrounds shown. The uncertainty in the background function was included in determining the uncertainty in the fitted peak areas.

more spectra at the same excitation energy (within ±15 keV). A second round of fits was made, fixing the energy of each peak at the average of the first-round fitting energy. The final selection of excitations was made by applying a χ-squared probability criterion to the fitted areas and the statistical errors for each presumed level. An "existence probability" was defined as one minus the χ-squared probability that a set of comparable areas would be generated by random fluctuations in a flat distribution of data points with the same average statistical errors. Only levels with existence probabilities greater than 90% are reported here.

The peak-fitting program calculated the areas under each of the elastic and inelastic peaks, integrating the radiative tail out to a distance of 200 keV from the peak center. The effect of the background polynomial was tested by estimating "high" and "low" plausible background functions, as shown in Fig. 5. The spectra were fitted using these two estimates as well as the best-fit background estimate; the difference between peak areas from the high and low background estimates was treated as an additional random contribution to the uncertainty in the peak area. As the estimated background functions did not correlate from spectrum to spectrum, this contribution was combined in quadrature with the statistical errors. The peak areas from the best-fit backgrounds were used to determine the cross sections and reduced transition probabilities of the inelastic transitions, as described in the following section.

III. CROSS SECTION CALCULATION

The experimental inelastic cross sections were calculated using the measured ratios of inelastic peak area to elastic peak area and a theoretical calculation of the elastic cross section. This procedure minimized the sensitivity to uncertainties in normalization effects such as

gas density, front-slit geometry and absolute counter efficiency. In addition, absolute elastic cross sections were also calculated from the data. Within their large uncertainties ($\approx \pm 15\%$), these agreed with the ^{36}Ar elastic cross sections of Finn *et al.* [22], confirming that most of the systematic effects of the experiment were understood. The ^{38}Ar elastic cross sections were similarly determined from the data. The ratio of ^{38}Ar to ^{36}Ar elastic cross sections, which is insensitive to all of the systematic uncertainties except gas density, was equal to unity within estimated errors.

To obtain the inelastic cross sections, the elastic-

TABLE I. Measured inelastic squared form factors $F^2(q)$, multiplied by 10^{-7}, for excitations measured in this experiment.

	^{36}Ar cross sections					
E_0 (MeV)=	25.45	34.72	41.26	55.78	46.29	62.89
θ=	153°	153°	153°	153°	117°	117°
q (fm^{-1})=	0.20	0.29	0.36	0.50	0.36	0.50
E_x (MeV)						
6.750	3.7(3.2)	0.2(1.6)	1.3(0.7)	1.1(0.5)	5.0(2.9)	7.7(3.7)
7.167	0.9(3.0)	1.4(1.7)	1.4(0.7)	2.4(0.5)	5.2(3.0)	10.2(3.7)
7.440	5.6(3.0)	16.6(1.9)	15.2(0.7)	17.0(0.7)	79.2(3.2)	103.4(4.2)
7.543	2.5(3.1)	4.1(1.8)	1.3(0.7)	0.6(0.6)	7.9(3.0)	4.6(3.0)
7.589	0.1(2.9)	4.1(1.9)	0.0(0.7)	1.2(0.6)	3.1(3.0)	7.7(3.2)
7.719	0.1(2.9)	4.0(1.9)	2.9(0.6)	3.3(0.5)	6.7(3.3)	9.7(4.1)
7.966	2.2(3.1)	3.1(2.0)	0.8(0.6)	1.4(0.5)	1.9(3.4)	7.2(4.2)
8.158	11.5(3.2)	5.0(2.0)	2.1(0.6)	1.0(0.5)	2.7(3.4)	2.5(1.6)
8.333	5.5(3.2)	1.0(1.8)	1.2(0.7)	2.8(0.5)	3.5(3.2)	7.0(3.4)
8.385	4.2(3.2)	3.9(1.9)	3.9(0.6)	3.8(0.6)	5.2(3.1)	7.1(3.2)
8.482	9.9(3.3)	0.4(1.8)	1.2(0.6)	1.2(0.5)	0.1(2.5)	5.8(3.7)
8.576	0.0(3.1)	0.7(1.9)	1.0(0.6)	2.0(0.5)	1.1(3.4)	7.8(3.9)
8.695	7.5(3.3)	2.9(2.0)	0.6(0.6)	2.2(0.5)	0.8(3.6)	10.8(4.2)
8.907	8.3(3.3)	2.5(2.0)	0.2(0.6)	0.5(0.5)	0.0(3.0)	7.2(4.2)
9.025	9.9(3.4)	3.3(1.9)	0.0(0.6)	1.8(0.5)	0.4(3.6)	10.6(4.0)
9.136	5.6(3.3)	0.0(1.7)	1.4(0.6)	2.8(0.5)	3.9(3.5)	9.2(3.9)
9.225	4.7(3.4)	5.0(2.0)	3.2(0.7)	3.8(0.5)	0.8(3.6)	9.2(4.0)
9.386	3.3(3.4)	0.5(1.9)	0.1(0.7)	1.7(0.5)	2.1(3.6)	10.3(3.9)
9.477	1.5(3.5)	0.4(1.6)	1.3(0.7)	1.4(0.5)	6.5(3.6)	14.2(3.8)
9.575	1.3(3.5)	1.2(1.9)	0.4(0.7)	1.6(0.5)	0.0(3.3)	7.8(4.1)
9.995	21.5(3.7)	15.8(2.0)	10.7(0.8)	5.1(0.6)	8.5(3.7)	8.8(3.7)
10.056	24.3(3.7)	1.3(1.8)	0.6(0.7)	1.5(0.5)	6.4(3.3)	11.7(3.2)
10.125	14.8(3.7)	2.8(1.8)	0.7(0.7)	1.6(0.5)	7.0(3.7)	8.6(3.8)
10.276	11.5(3.7)	2.5(1.8)	0.6(0.7)	0.8(0.5)	0.0(3.1)	5.4(3.6)
10.335	10.8(3.8)	2.7(1.8)	1.2(0.7)	1.3(0.5)	8.7(3.6)	12.1(3.5)
10.434	0.1(3.6)	3.5(1.8)	2.4(0.7)	2.2(0.5)	0.4(4.0)	6.0(4.1)
10.615	0.8(3.8)	5.4(1.9)	0.0(0.6)	0.6(0.5)	0.0(3.9)	5.6(3.9)
10.719	10.2(3.9)	4.3(1.8)	0.7(0.7)	1.4(0.5)	0.0(3.2)	3.7(2.7)
10.764	6.4(3.9)	5.6(1.9)	1.4(0.7)	0.1(0.5)	1.1(3.7)	3.5(2.5)
11.177	18.2(4.0)	13.1(1.9)	10.5(0.7)	5.7(0.6)	19.3(4.1)	15.8(3.9)
11.285	0.0(3.5)	0.5(1.7)	0.8(0.7)	1.4(0.5)	7.3(4.1)	2.4(2.9)
11.384	2.3(4.1)	1.6(1.8)	2.0(0.7)	1.1(0.5)	5.5(4.1)	0.8(5.9)
11.515	3.0(4.1)	0.1(1.7)	2.1(0.7)	2.4(0.6)	6.2(4.0)	6.5(8.8)
11.594	10.4(4.2)	1.0(1.7)	2.6(0.7)	2.8(0.6)	1.5(4.1)	5.5(9.3)
11.745	1.2(4.2)	1.4(1.7)	1.1(0.7)	2.1(0.6)	1.9(4.4)	8.0(11.7)
11.946	5.0(4.2)	0.7(1.8)	1.7(0.7)	2.0(0.6)	1.8(4.4)	4.7(13.9)
12.066	11.3(4.3)	0.3(1.7)	2.4(0.7)	2.2(0.6)	0.8(4.3)	
12.184	8.5(4.3)	1.8(1.8)	0.9(0.7)	1.2(0.6)	7.5(4.0)	
12.420	0.2(4.3)	2.0(1.8)	1.3(0.7)	1.3(0.6)	6.5(4.1)	
12.601	7.1(4.4)	3.7(1.9)	2.9(0.7)	4.0(0.7)	12.1(4.2)	
12.801	10.3(4.4)	5.1(1.9)	1.6(0.7)	0.4(0.7)	0.9(4.0)	
13.070	2.1(4.5)	1.2(1.9)	2.3(0.7)	2.1(0.7)	11.2(4.1)	
13.201	4.2(4.5)	5.3(2.0)	2.1(0.7)	0.9(0.7)	4.2(4.0)	
13.481	5.9(4.7)	3.5(2.0)	2.1(0.7)	0.7(0.9)	3.9(4.7)	
13.740	0.4(5.0)	6.0(2.1)	0.1(0.7)	0.3(0.7)	4.5(3.9)	
13.800	0.0(5.7)	1.1(2.1)	3.3(0.8)	2.0(0.7)	7.4(3.7)	

TABLE I. *(Continued).*

	^{38}Ar cross sections				
E_0 (MeV)=	25.45	34.72	41.26	55.78	46.29
θ=	153°	153°	153°	153°	117°
q (fm^{-1})=	0.20	0.29	0.36	0.50	0.36
E_x (MeV)					
7.381	6.8(6.0)	0.5(2.0)	3.7(1.3)	2.2(0.7)	7.5(4.0)
7.721	0.9(5.3)	1.5(2.2)	3.2(1.5)	1.3(0.8)	6.1(4.0)
7.877	17.6(5.3)	6.2(2.2)	7.3(1.5)	6.5(1.1)	27.1(4.0)
8.240	6.4(6.0)	4.5(2.3)	3.7(1.3)	2.4(0.7)	16.8(3.8)
8.313	10.5(4.8)	0.4(2.1)	2.9(1.3)	0.7(0.7)	1.6(3.5)
8.409	0.6(4.8)	0.0(2.2)	4.0(1.5)	2.0(0.8)	10.3(3.9)
9.431	0.5(5.0)	1.5(3.0)	4.7(1.5)	2.2(0.8)	1.6(3.8)
9.603	0.2(4.1)	2.4(2.8)	4.7(1.4)	1.8(0.7)	10.7(3.8)
9.645	0.8(6.0)	0.0(2.1)	2.0(1.5)	1.0(0.7)	9.5(4.0)
10.058	0.3(4.0)	2.2(2.4)	3.2(1.4)	1.8(0.7)	13.1(3.8)
10.118	6.0(8.3)	2.5(2.1)	3.8(1.4)	0.7(0.7)	10.2(3.8)
10.207	0.2(5.5)	4.8(2.6)	2.1(1.5)	0.9(0.8)	5.9(3.8)
10.495	6.1(7.4)	4.3(2.2)	2.8(1.3)	0.0(0.5)	0.2(3.4)
10.673	9.7(7.3)	3.3(2.3)	3.0(1.4)	3.3(0.9)	3.5(3.9)
11.556	9.7(7.5)	5.4(2.4)	2.6(1.6)	0.0(0.6)	2.7(4.3)
11.716	7.2(8.3)	5.2(2.6)	4.0(1.6)	0.4(0.8)	2.3(3.7)
11.855	13.7(9.0)	4.0(2.3)	4.2(1.7)	0.0(0.7)	4.4(4.4)
12.000	10.9(9.2)	5.8(2.1)	1.6(1.3)	0.1(0.8)	0.7(3.9)
12.134	13.5(7.6)	3.0(2.0)	3.1(1.5)	1.1(0.8)	1.1(3.2)
12.369	13.4(7.8)	4.0(2.8)	2.7(1.5)	0.8(0.8)	1.4(4.2)
13.891	0.2(7.4)	4.5(2.9)	1.8(1.5)	1.9(0.8)	0.8(3.8)
13.967	3.4(9.3)	0.1(2.3)	4.0(1.6)	1.6(0.9)	0.2(3.7)
14.066	0.5(9.4)	5.6(3.2)	6.4(1.8)	2.9(1.0)	6.9(3.6)
14.206	17.3(7.8)	0.9(2.9)	3.5(1.7)	0.0(0.7)	6.7(3.5)
14.924	16.8(12.8)	6.4(2.6)	3.7(7.1)	1.2(2.1)	34.9(24.0)

to-inelastic peak area ratios, adjusted for small differences in the radiative corrections, were multiplied by theoretical elastic-scattering cross sections. The latter were determined by a distorted-wave Born approximation (DWBA) phase-shift calculation, using a two-parameter Fermi charge distribution. The charge parameters for ^{36}Ar were taken from Ref. [22]. For ^{38}Ar, in which no charge radius measurements exist, we used an average of the parameters [22] for ^{36}Ar and ^{40}Ar; the results differed only insignificantly from the ^{36}Ar values. The experimental inelastic cross sections obtained in this manner are listed in Table I.

IV. TRANSITION MULTIPOLARITIES AND STRENGTHS

Transition multipolarities were assigned to the observed excitations by the traditional "model-independent" analysis used in electron scattering at low-momentum transfers [23]. The data were corrected for Coulomb distortion, then compared with expressions for the cross section in PWBA. The Coulomb distortion corrections were calculated with the DWBA code DENS [24], using shell-model amplitudes for $M1$ transitions and single-particle amplitudes for the other magnetic multipoles.

In PWBA, and neglecting recoil, the cross section may be written

$$\frac{d\sigma}{d\Omega} = \sigma_M F^2(q) = \left[\frac{Ze^2\cos(\theta/2)}{2E_0\sin^2(\theta/2)}\right]^2 F^2(q)$$
$$= \sigma_M\left\{\left(\frac{\Delta^2}{q^2}\right)^2 F_L^2(q) + \left[\frac{1}{2}\frac{\Delta^2}{q^2} + \tan^2\frac{\theta}{2}\right]F_T^2(q)\right\} \quad (1)$$

where σ_M is the Mott cross section; q and Δ are the three- and four-momentum transfers respectively; F, F_L, and F_T are the total, longitudinal, and transverse form factors respectively; E_0 is the incident electron energy, and θ is the scattering angle.

In PWBA, F_L^2 and F_T^2 can be written as

$$F_L^2(q) = \frac{4\pi}{Z^2}\sum\frac{q^{2\lambda}}{([2\lambda+1]!!)^2}B(C\lambda,q), \quad (2a)$$

$$F_T^2(q) = \frac{4\pi}{Z^2}\sum\frac{(\lambda+1)q^{2\lambda}}{\lambda([2\lambda+1]!!)^2}[B(E\lambda,q)+B(M\lambda,q)], \quad (2b)$$

where the sum runs over all multipolarities λ which contribute to the electro-excited transition, and $B(C\lambda,q)$, $B(E\lambda,q)$, and $B(M\lambda,q)$ are the Coulomb (longitudinal), transverse electric, and magnetic reduced transition probabilities, respectively. The factor $q^{2\lambda}$ in Eqs. (2) shows that states of high multipolarity will become more significant relative to low-multipolarity states as the momentum transfer increases. For the low-q range characteristic of these experiments, the $B(X\lambda,q)$ can be expanded in terms of their respective radial moments as follows:

TABLE II. Multipolarities and transition probabilities for ^{36}Ar. Transitions identified in the present experiment are grouped by multipolarity assignment and listed by excitation energy E_x. *Column 1*: Excitation energies have an uncertainty of 8 to 15 keV. *Column 2*: Reduced transition probabilities $B(X\lambda,\omega)$ and their uncertainties. Starred values are the results of preliminary fits which are described in the text; they have not been used in later sections of this paper. Note that $90.416\mu_N^2 = 1\ e^3\text{fm}^2$. *Column 3*: Transition radius, and its uncertainty, when it could be determined to ± 0.7 fm or better; if the column is blank, the fit used $R_{\text{tr}} = 3.6$ fm (for $\lambda = 1$), 3.8 fm ($\lambda = 2$), or 4.0 fm ($\lambda = 3$). *Column 4*: χ-squared per degree of freedom χ^2_ν of the fit to $\sqrt{B(X\lambda,q)}$ vs q^2 for the given multipole. The number of degrees of freedom is 5 for levels below 12 MeV in ^{36}Ar, 4 for all others. *Column 5*: The multipolarity assignment agrees with ("*a*") or disagrees with ("*d*") possible spin-parity assignments reported in Ref. [26]. *Column 6*: Some peaks were found to consist of a mixture of multipolarities; an $X\lambda$ entry here indicates the multipolarity of the transition which was unresolved from the tabulated transition. The $B(X\lambda,\omega)$ listed in column 2 is the separated strength of the transverse transition. Note that ν is reduced by 1. *Column 7*: The next most likely multipolarity assignments for each transition and the χ^2_ν of the fit (or the transition radius, in the case of those fits where the radius was measured). Assignments that agree with possible spin-parity assignments from Ref. [26] are underlined.

$M1$ transitions

E_x (MeV)	$B(M1,\omega)$ (μ_N^2)	R_{tr} (fm)	χ^2_ν	Agree	Mix	Alt. (χ^2_ν)
7.440	0.126(0.024)		1.68	*a*	$+C2$	
8.158	⋆0.207(0.056)	4.1(0.4)	2.04	*a*		$C1(R = 7.2 \pm 0.4)$
	⋆0.157(0.024)		1.89	*a*		$C1$(7.33)
	0.087(0.018)		1.55	*a*	$+C3$	
8.482	0.123(0.027)		3.06			$C1$(3.95)
9.995	⋆0.532(0.056)	3.5(0.2)	1.11	*a*		$M2(R = 6.2 \pm 0.1)$
	0.567(0.029)		0.99	*a*		$C1$(27.78)
10.276	0.121(0.030)		2.15			$C1$(4.51)
10.615	0.119(0.049)		2.42			$C1$(2.86)
10.719	0.140(0.029)		2.51	*d*		$C1$(4.34)
10.764	0.120(0.028)		1.94			$C1$(3.93)
11.177	⋆0.447(0.050)	3.0(0.2)	3.20			$M2(R = 6.0 \pm 0.2)$
	⋆0.574(0.028)		4.04			$C1$(18.77)
	0.310(0.025)		0.11		$+C2$	
11.384	0.106(0.024)		0.37			$C1$(0.6),$M2$(0.9)
12.066	0.162(0.029)		2.21			$C1$(3.51)
12.801	⋆0.291(0.076)	5.5(0.5)	1.17			$M2(R = 7.9 \pm 0.5)$
	0.126(0.029)		2.12			$C1$(4.96)
13.201	⋆0.175(0.076)	4.3(0.7)	0.59			$C1(R = 6.8 \pm 1.1)$
	0.131(0.028)		0.55			$C1$(2.46)
13.481	0.115(0.028)		0.25			$C1$(1.59)
13.740	0.123(0.041)		2.48			$C1$(3.80)
13.800	0.173(0.031)		1.23			$M2$(1.65)

$M2$ transitions

E_x (MeV)	$B(M2,\omega)$ (fm^2 μ_N^2)	R_{tr} (fm)	χ^2_ν	Agree	Mix	Alt.
7.719	⋆29.3(10.0)	4.0(0.7)	1.55	*d*		$M3(R = 6.9 \pm 0.5)$
	27.1(3.0)		1.25	*d*		$C2$(2.90)
8.333	21.1(3.1)		1.96	*a*		$M3$(2.55)
8.385	⋆43.4(12.0)	4.4(0.5)	0.48			$M3(R = 7.3 \pm 0.3)$
	32.7(3.2)		0.61			$M1$(5.16)
9.136	21.4(3.1)		2.55	*d*		$\underline{C2}$(2.75)
9.225	31.7(3.2)		1.43	*d*		$C1$(4.70)
10.434	20.9(3.2)		0.78	*a*		$C1$(1.86)
11.515	20.7(3.5)		0.75			$C2$(1.03)
11.594	⋆41.4(16.)	4.9(0.7)	3.35			$M1(R = 1.4 \pm 1.2)$
	⋆25.2(3.7)		2.99			$M1$(2.98)
	15.5(4.2)		1.73		$+C1$	
11.745	15.5(3.3)		0.26			$M3$(0.4),$C2$(0.5)
11.946	16.8(3.7)		0.70			$M1$(1.39)

TABLE II. *(Continued).*

Longitudinal transitions

E_x (MeV)	$X\lambda$	Agree	Mix	Alt.
6.750	$C1$	d		$\underline{C2}$
7.167	$C2$	a		$C3$
7.440	$C2$	a	$+M1$	
7.543	$C1$			
7.589	$C3$			
7.966	$C2$	d		$\underline{M2}, C1$
8.158	$C3$		$+M1$	
8.576	$C3$	d		$\underline{C2}, M3, M2$
8.695	$C3$		$+M1$	
8.907	$C3$			
9.025	$C1$	d		$\underline{C2}$
9.386	$C3$	a		$\underline{C2}$
9.477	$C2$	a		$C3$
9.575	$C3$	d		$\underline{C2}$
10.056	$C1$	a		$C0$
10.125	$C1$	a		$\underline{C2}$
10.335	$C1$	d		$\underline{C2}$
11.177	$C2$		$+M1$	
11.285	$C2$			$C1$
11.594	$C1$		$+M2$	
12.184	$C1$			$M1, C0$
12.420	$C1$			$C2$
12.601	$C3$			
13.070	$C1$			$C2$

$$\sqrt{B(C\lambda,q)} = \sqrt{B(C\lambda,0)}\left\{1 - \frac{q^2\langle r_C^2\rangle}{2(2\lambda+3)} + \frac{q^4\langle r_C'^4\rangle}{8(2\lambda+3)(2\lambda+5)} - \cdots\right\}, \tag{3a}$$

$$\sqrt{B(E\lambda,q)} = \frac{1}{q}\sqrt{\lim_{q\to 0}\{q^2 B(E\lambda,q)\}}\left\{1 - \frac{\lambda+3}{\lambda+1}\frac{q^2\langle r_E^2\rangle}{2(2\lambda+3)} + \cdots\right\}, \tag{3b}$$

$$\sqrt{B(M\lambda,q)} = \sqrt{B(M\lambda,0)}\left\{1 - \frac{\lambda+3}{\lambda+1}\frac{q^2\langle r_M^2\rangle}{2(2\lambda+3)} + \frac{\lambda+5}{\lambda+1}\frac{q^4\langle r_M'^4\rangle}{8(2\lambda+3)(2\lambda+5)} - \cdots\right\}, \tag{3c}$$

where r_X and r'_X ($X = C$, E, or M) are given in Eqs. (11)–(13) of Ref. [25]. The first moments, $r_X \equiv \langle r_X^2\rangle^{1/2}$, called the transition radii, are usually slightly larger than the ground-state charge radius ρ and smaller than 1.2ρ (for $X\lambda = M1$) [23].

Expressions (3a) and (3c) are used to determine the multipolarity of the measured transitions. Because both ^{36}Ar and ^{38}Ar have spin-0 ground states, a transition must be either purely magnetic (M) or purely electric (C and E). Values of $B(X\lambda,q)$ were calculated from the experimentally measured cross sections assuming in turn that the multipolarity $X\lambda$ of the transition was $M1$, $M2$, $M3$, $C1$, $C2$, and $C3$. (States with $\lambda \geq 3$ were not expected to be seen at these low-momentum transfers, but the possibility $\lambda = 3$ was considered for thoroughness.) Transverse electric ($E\lambda$) contributions were not considered because the contribution of the Coulomb transition usually dominates. The number and precision of data points did not allow a separation of C and E contributions.

The angular dependence of the transverse part of Eq. (1) was used to separate transverse (magnetic) transitions from those which were predominantly longitudinal (Coulomb). The measurements at 117° and 46 MeV corresponded to the same momentum transfer, $q \approx 0.36$ fm^{-1}, as the measurements at 153° and 41 MeV. A second forward-angle run at 117° and 63 MeV, to match the 0.50 fm^{-1} momentum transfer of the 56 MeV run at 153°, was terminated early because of accelerator troubles, giving only a partial spectrum on ^{36}Ar and no data on ^{38}Ar. At any fixed q value, if a transition is purely magnetic, the $B(M\lambda,q)$ values calculated from the cross sections

will agree in PWBA, while the calculated $B(C\lambda,q)$ value from 117° will be about six times smaller than that from 153°. In contrast, for a pure Coulomb transition, the $B(C\lambda,q)$ will agree, while the $B(M\lambda,q)$ from 117° will be about six times larger than that from 153°. In most cases the assignment of longitudinal or transverse was unambiguous.

The values of $\sqrt{B(X\lambda,q)}$ were fitted as a function of q^2 using Eqs. (3a) and (3c) with λ=1,2,3. Initially, a good fit to the data [with a transition radius within 10% of $(1+0.09\lambda)\rho$] was taken to indicate that the transition has the corresponding multipolarity. Because most of the levels were too weak for the fit to determine reliably the transition radius, the transition radii for the final round of fits were held fixed at the values $r_M = r_C = 3.60$, 3.80, and 4.00 fm for $\lambda = 1$, 2, and 3 fits respectively. Results from both preliminary (variable-radius) and fixed-radius fits were listed in Table II; the subsequent analysis uses only the fixed-radius fits. The coefficient of the q^4 term in the expansions was taken as $r'^4_X = 1.14 r^4_X$ for all multipoles; the factor 1.14 was obtained from the DWBA calculations using DENS.

If the statistical uncertainties of the data points were not too large, the determination of multipolarity was unambiguous. For the weaker transitions, the multipole assumption which fit the data points with the smallest χ squared was selected. The extrapolation of the curve of correct multipolarity to the photon point $q = \omega$ then gives the value of the transition strength $B(X\lambda,\omega)$. Figure 6 shows examples of the multipolarity fits.

A few transitions appeared to fit no single multipolarity hypothesis, presumably because they consisted of two unresolved peaks. For these transitions, the experimental form factors were fitted using a sum of contributions

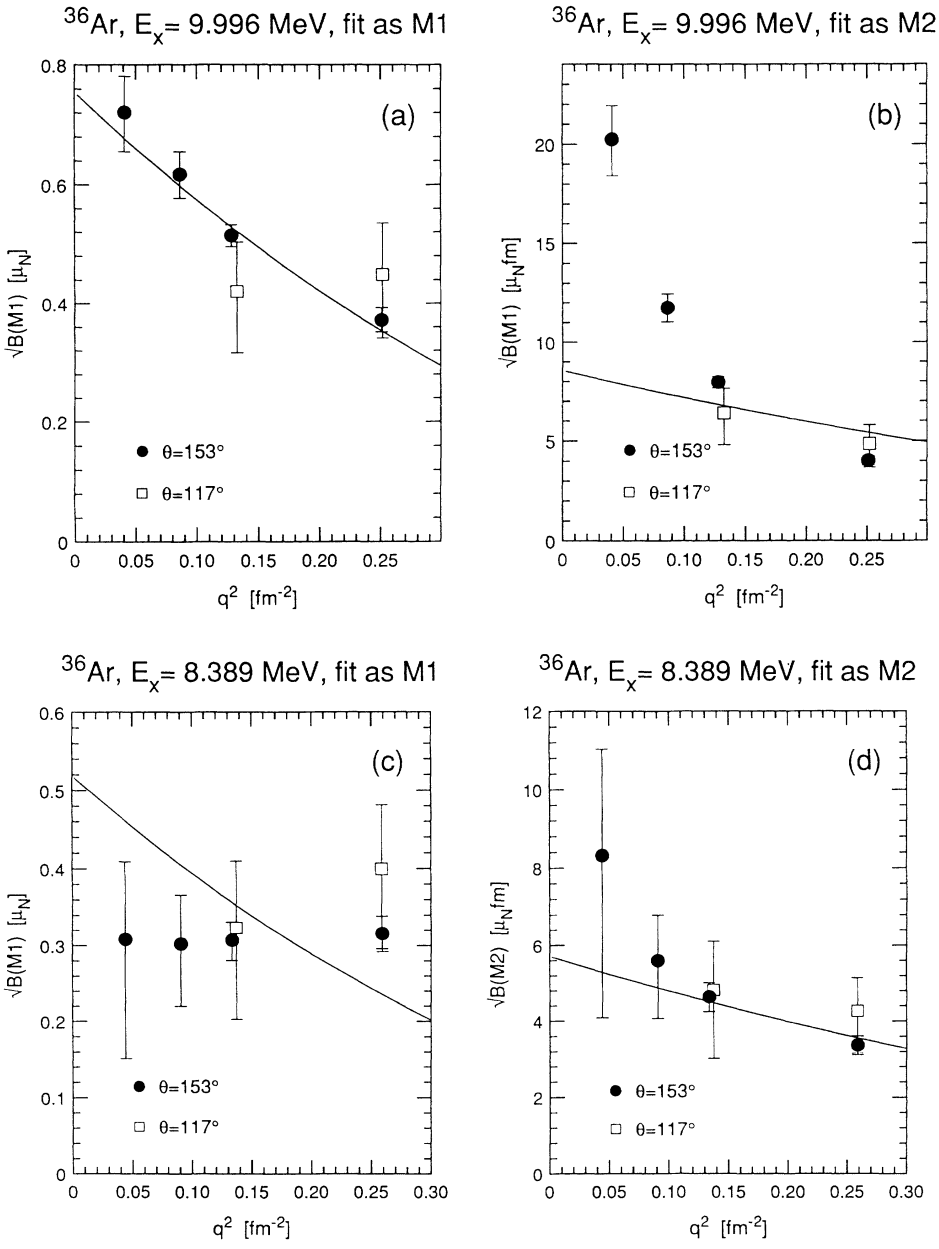

FIG. 6. Examples of fits of $\sqrt{B(X\lambda,q)}$ vs q^2, used in determining transition multipolarity and strength. (a) An $M1$ transition fitted as an $M1$ and (b) as an $M2$. (c) An $M2$ transition fitted as an $M1$ and (d) as an $M2$. The $B(X\lambda,q)$ values are corrected for Coulomb distortion.

from two transition multipolarities, according to Eqs. (1) and (2).

Tables II and III list the values of $B(M\lambda,\omega)$ for transitions identified as $M1$ and $M2$ in ^{36}Ar and ^{38}Ar. All of these transitions had "existence probabilities" of at least 90%. As expected at these low momentum transfers, no convincing $M3$ excitations were found. Tables II and III also indicate whether the multipolarities assigned to transitions measured in this experiment agree with spins and parities reported in Ref. [26]. Because complete forward-angle data were taken at only one value of momentum transfer, no reliable separation of transverse electric from Coulomb contributions was possible. Thus the determination of $B(C\lambda,\omega)$ for the primarily longitudinal excitations was subject to additional uncertainties, and these values are not included in Tables II and III. Approximate values of $B(C\lambda,\omega)$ can be found in Ref. [14].

V. COMPARISON WITH THEORY

The distribution of $M1$ transition strength in ^{36}Ar predicted by shell-model (SM) calculations is shown in the upper part of Fig. 7(a), and the experimental strengths determined in this experiment (in the range $6.5< E_x <$ 15 MeV) in the lower part. Figure 7(b) shows the corresponding distributions for ^{38}Ar.

The SM calculations were carried out in the full $1s0d$ model space using the Wildenthal effective interaction [27,28]. This interaction was obtained from a fit of the $1s0d$-shell single-particle energies and two-body matrix elements to 447 binding energies and excitation energies in the mass region A=17–39 [27,28]. The spectroscopic properties of the $1s0d$-shell nuclei are well reproduced. In particular, the magnetic moments and $M1$ transition strengths are well reproduced when an empirical effective

TABLE III. Multipolarities and transition probabilities for ^{38}Ar. See Table II for an explanation of symbols.

$M1$ transitions

E_x (MeV)	$B(M1,\omega)$ (μ_N^2)	R_{tr} (fm)	χ^2_ν	Agree	Mix	Alt.
7.381	0.207(0.042)		1.30	a		$M2$(1.85)
7.721	0.145(0.042)		0.71			$M2$(0.95),$C1$(2)
7.877	⋆0.560(0.050)		10.0			$C1$(5.97)
	0.139(0.043)		1.19		$+C2$	
8.313	0.138(0.030)		1.21			$C1$(3.50)
9.431	0.204(0.046)		1.11			$M2$(1.12)
10.207	0.142(0.042)		0.55			$C1$(1.15)
10.495	0.127(0.040)		0.87			$C1$(2.68)
11.556	0.159(0.048)		0.89			$C1$(3.16)
11.716	0.168(0.045)		0.56			$M2$(3.06)
11.855	0.188(0.050)		1.02			$M2$(3.29)
12.000	0.144(0.043)		1.45			$C1$(3.71)
12.134	0.149(0.042)		0.90			$M2$(3.42)
12.369	0.148(0.045)		0.86			$C1$(3.03)
13.891	0.148(0.044)		0.67			$M2$(0.8),$C1$(1.7)
13.967	0.159(0.050)		0.81			$M2$(1.22)
14.066	0.291(0.053)		0.34			$M2$(2.12)
14.206	0.205(0.057)		2.32			$C1$(4.49)

$M2$ transitions

E_x (MeV)	$B(M2,\omega)$ (fm^2 μ_N^2)	R_{tr} (fm)	χ^2_ν	Agree	Mix	Alt.
10.673	29.0(5.9)		1.07	d		$M1$(1.52)

Longitudinal transitions

E_x MeV	$X\lambda$	Agree	Mix	Alt.
7.877	$C2$	a	$+M1$	$C1$
8.240	$C1$	a		$C2$
8.409	$C2$			$C1$
9.603	$C1$	a		$M1$
9.645	$C1$			$C2$
10.058	$C1$	d		$C2$
10.118	$C1$			
14.924	$C1$			$M1$

TABLE IV. Summary of the energy distribution of $M1$ strength in ^{36}Ar and ^{38}Ar. The centroid $\langle E_x \rangle$ and RMS width σ_E are defined in the text. The "Experiment" values are calculated from the $M1$ transitions identified in this experiment, as listed in Tables II and III. The "Shell model" values come from the "free-nucleon" and "effective operator" versions of the $1s0d$-shell calculations described in the text.

		Shell model (free nucleon)		Shell model (effective operators)	
	Experiment	(all E_x)	(E_x < 15 MeV)	(all E_x)	(E_x < 15 MeV)
^{36}Ar					
Centroid (MeV)	11.04	12.03	11.23	12.14	10.98
RMS width (MeV)	1.74	2.52	1.67	2.86	1.56
^{38}Ar					
Centroid (MeV)	11.28	10.62	10.62	10.55	10.55
RMS width (MeV)	2.32	[a]	[a]	[a]	[a]

[a]Calculations for ^{38}Ar give only a strong state at 10.623 MeV and a very weak state at 5.555 MeV; the RMS width of this distribution is meaningless.

one-body operator is introduced [10,13,29]. This effective operator takes into account higher-order configuration mixing from configurations outside the $1s0d$ shell as well as the mesonic exchange currents [11–13].

We compare our experimental results with calculations that use the free-nucleon operator as well as the effective operator (from the "moments plus $M1$ decay" row of Table II in Ref. [10]). Since the empirical effective $M1$ operator was based primarily on transitions between low-lying states, the higher-lying states measured in this experiment provide an important test of the model assumptions.

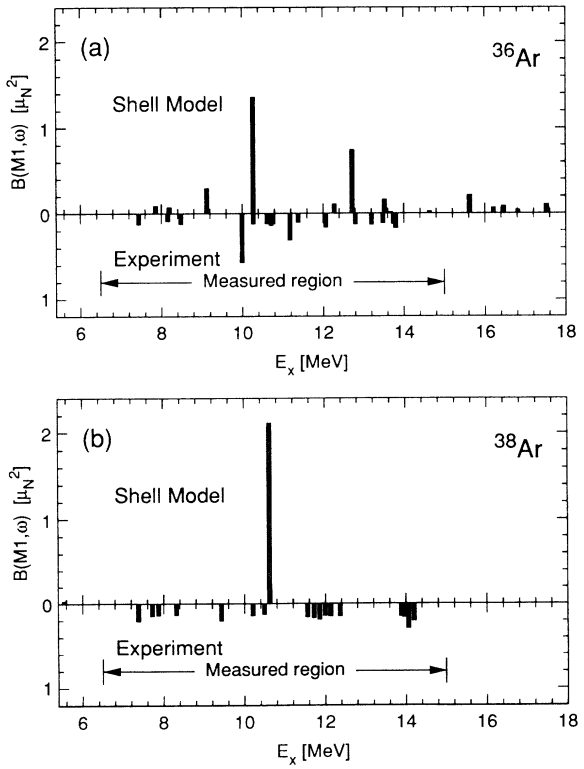

FIG. 7. (a) Theoretical and experimental $M1$ strength in ^{36}Ar. The shell-model calculations are the $1s0d$-shell calculations described in the text, using the effective $M1$ operator. (b) Theoretical and experimental $M1$ strength in ^{38}Ar.

The theoretical $M1$ strengths plotted in Fig. 7 are calculated using the effective $M1$ operators. Compared to the calculation using the free-nucleon operator, the use of the effective operators reduces the $M1$ strengths by an average of about 30% in ^{36}Ar and by nearly a factor of 2 in ^{38}Ar.

Table IV compares the centroids and widths of the $M1$ strength distributions for ^{36}Ar and ^{38}Ar. The centroids

$$\langle E_x \rangle = \left(\sum\{E_x \cdot B\}\right) \Big/ \left(\sum B\right)$$

and RMS widths

$$\sigma_{E_x} = \left[\sum\{(E_x - \langle E_x \rangle)^2 \cdot B\} / \left(\sum B\right)\right]^{1/2}$$

are presented for the experimental results, for the SM results, and for the SM results with the sum restricted to the experimentally measured region 6.5 MeV< E_x < 15 MeV.

There is at least qualitative agreement between the distributions for ^{36}Ar in Fig. 7, but the measured transition strengths are somewhat smaller and more fragmented than those predicted. Note that the theory predicts substantial $M1$ strength between 15 and 20 MeV, beyond the region of the measurements.

For ^{38}Ar, the shell model predicts only a single strong $M1$ transition at 10.623 MeV (plus a very weak state at 5.55 MeV). In contrast, the data show a cluster of weak transitions in the energy region near the predicted strong transition, although (as discussed in the following section) the total observed strength is close to that predicted.

The prediction that the $M1$ strength in ^{38}Ar should be concentrated in a single transition results from the fact that, in an exclusively $1s0d$-shell calculation, ^{38}Ar has a closed neutron shell with a simple $(1d_{3/2})^{-2}$ pro-

TABLE V. Total $M1$ transition strength $\sum B(M1,\omega)$ in ^{36}Ar and ^{38}Ar, in units of μ_N^2. The IPM sum rule is given by Eq. (4). The "Shell model" results are from the $1s0d$-shell calculations described in the text.

	IPM	Shell model (free nucleon)		Shell model (effective operators)		
	sum rule	(all E_x)	($E_x \leq 15$ MeV)	(all E_x)	($E_x \leq 15$ MeV)	Experiment
^{36}Ar	10.22	5.13	4.37	3.54	2.86	2.65±0.12
^{38}Ar	6.03	4.10	4.10	2.14	2.14	2.86±0.18

ton configuration [10]. If fp-shell states were to be included in the calculation, not only would a higher level density and additional spreading result, but the total $M1$ strength would probably increase. It appears that a pure $1s0d$-shell calculation, is inadequate to predict the distribution of $M1$ strength in nuclei so close to the closure of the shell.

VI. COMPARISON WITH SUM RULES

The independent-particle model (IPM) predicts that the sum over isovector and isoscalar $M1$ transitions for a pure $d_{5/2} \rightarrow d_{3/2}$ excitation is [30]

$$\sum B(M1,\omega) = \frac{9}{20\pi}\{[n_p(g_p^s - g_p{}^l)]^2 + [n_n(g_n^s - g_n{}^l)]^2\}, \quad (4)$$

where n_p and n_n are the number of active (valence) proton and neutron particles or holes; i.e., 2 and 2 for ^{36}Ar, 2 and 0 for ^{38}Ar. The superscripts s and l denote spin and orbital g factors, respectively. Using the free-particle g factors, the sum is $10.22\mu_N^2$ for ^{36}Ar and $6.03\mu_N^2$ for ^{38}Ar. The full $0s1d$-shell calculations with the free-nucleon operator give substantially smaller values for the total $M1$ strength, and the use of the effective $M1$ operator reduces the predictions still further, as seen in Table V.

Evaluating the summed experimental strength was difficult, because the statistical uncertainty of the data prevented us from detecting transitions with $B(M1,\omega)$ less than about $0.1\mu_N^2$ in ^{36}Ar and less than about $0.14\mu_N^2$ in 38Ar. To allow a visual estimate of the possible $M1$ strength in transitions below the detection threshold, the experimental $B(M1,\omega)$ values were ordered by size, from largest to smallest, and partial sums were obtained by summing the $B(M1)$ values from the largest down to $B_{\min}$. The partial sums for ^{36}Ar and ^{38}Ar vs $B_{\min}$ in the low-$B_{\min}$ region are plotted in Figs. 8(a) and 8(b), respectively. The "shell model" histograms are the results of similar partial sums of the $B(M1)$ values obtained in the shell model described in Sec. V, and are shown both for all energies and for energies predicted to be in the measured energy region ($E_x < 15$ MeV).

For ^{36}Ar, there is no systematic trend to the evolution of $\sum B(M1)$ vs $B_{\min}$ for the various theoretical distributions, and it is untenable to extrapolate the steep slope of the experimental distribution to lower $B_{\min}$. A linear extrapolation to $B_{\min}$=0, giving $\sum B(M1) \approx 4.2\mu_N^2$, might be viewed as an upper limit to plausible estimates for total $M1$ strength in ^{36}Ar, but in the absence of a sensible model, we use the sum of observed strength, $\sum B(M1) = 2.65 \pm 0.12\mu_N^2$, as our best estimate for the total. For ^{38}Ar there is even less theoretical guidance for estimating the missing strength, so again we use the sum of observed strengths, $\sum B(M1) = 2.86 \pm 0.18\mu_N^2$, for the total.

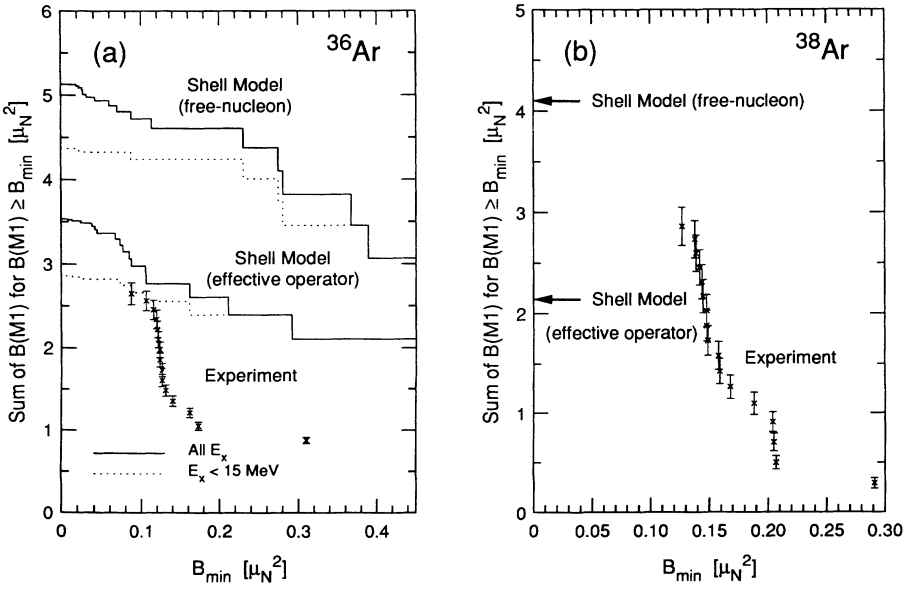

FIG. 8. Partial sums of $B(M1,\omega)$ vs $B_{\min}$. (a) ^{36}Ar. Data points: this experiment. Solid histograms: shell-model calculations using free-particle and effective nucleon operators. Dotted histograms: shell-model calculations with excitation energy restricted to the region measured, $E_x < 15$ MeV. (b) ^{38}Ar. Data points: this experiment. The two arrows indicate the shell model predictions.

TABLE VI. Total energy-weighted $M1$ transition strength $\sum E_x B(M1,\omega)$, in units of MeV μ_N^2. The Kurath sum rule is given by Eq. (5). The "Shell model" values are from the $1s0d$-shell calculations described in the text.

	Kurath	Shell model (free-nucleon)		Shell model (effective operators)		
	sum rule	(all E_x)	($E_x \leq 15$ MeV)	(all E_x)	($E_x \leq 15$ MeV)	Experiment
^{36}Ar	106.1	61.7	49.1	42.9	31.4	29.3±1.4
^{38}Ar	53.1	43.6	43.6	22.6	22.6	32.3±2.2

The resulting $M1$ strength sums are shown in Table V. As the experiment extended only up to 15 MeV in excitation energy, it is most reasonable to compare the experimental sum with the sum of only those shell-model transitions whose excitation energies fall in the measured region ($E_x < 15$ MeV), and these are also shown in Table V. The "running sums" of the experimental and theoretical $M1$ strengths vs excitation energy are shown in Fig. 9. For ^{36}Ar, the measured experimental sum is (93 ± 5)% of the effective-operator shell-model value in the measured energy region. In ^{38}Ar, for which only one significant SM transition was predicted, the restriction on E_x does not affect the SM sums. The sum of measured strengths is (134±6)% of the effective-operator shell-model calculation.

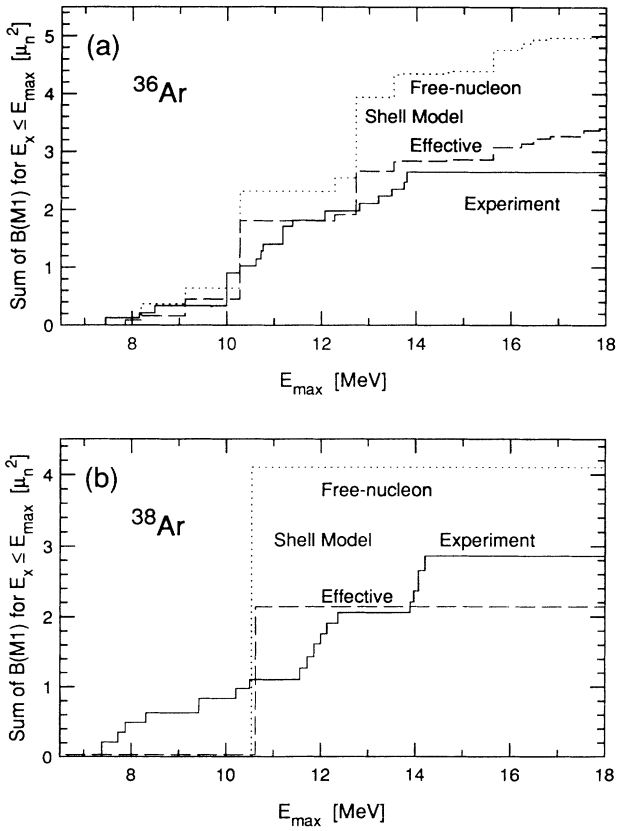

FIG. 9. Running sums of $B(M1,\omega)$ vs maximum excitation energy. Solid histograms: this experiment. Dotted histograms: shell-model calculations with free-nucleon operator. Dashed histograms: shell-model calculation with effective operator. (a) ^{36}Ar. (b) ^{38}Ar.

It is also of interest to compare our results with the energy-weighted sum rule of Kurath, which is derived using a Hamiltonian which includes spin-orbit coupling and a central-force two-body interaction [31]

$$\sum \omega_j B(M1,\omega)_j \approx -a(\mu_n + \mu_p + \tfrac{1}{2})^2 \langle g| \sum l_i s_i |g\rangle, \quad (5)$$

where $B(M1,\omega)$ and ω_j are, respectively, the reduced transition probability and the excitation energy of the jth level, and a is a spin-orbit coupling parameter which we take as $a = -2.03$ MeV for the $1s0d$-shell, based on the 5.08 MeV state and ground state of ^{17}O. The values shown in Table VI for ^{36}Ar and ^{38}Ar are obtained from Eq. (5) by calculating the expectation value $\langle g| \sum ls |g\rangle$ assuming a spherical nucleus in the extreme single-particle model. The shell model and experimental results are based on $B(M1,\omega)$ and ω_j from the SM and the data, respectively, with the same conditions as the corresponding columns of Table V.

The pattern of saturation of the Kurath sum rule is similar to that of the unweighted sum rule of Eq. (4). The measurements and the shell-model calculations for ^{36}Ar and ^{38}Ar are (93±5)% and (143 ± 7)%, respectively, of the effective-operator shell-model results when restricted to $E_x < 15$ MeV.

VII. CONCLUSIONS

Our study of low-multipolarity magnetic transitions in ^{36}Ar and ^{38}Ar in the 6.5 to 15 MeV excitation energy region, measured with significantly higher resolution than earlier work [9], has shown that considerable fragmentation of the $M1$ transition strength occurs in both nuclei.

For ^{36}Ar the observed fragmentation is in distinct contrast to the concentration of $M1$ strength found in the lighter self-conjugate nuclei, ^{20}Ne, ^{24}Mg, and ^{28}Si, although for ^{32}S some fragmentation is noticeable [8]. The sum of observed $M1$ transition strengths for ^{36}Ar is (93±5)% of the sum calculated in the measured energy region using the effective $M1$ operator.

In ^{38}Ar, the $M1$ transition strength was more severely fragmented. This continues the trend found in other $A = 4N + 2$ nuclei of the $1s0d$ shell. Although shell-model calculations based only on the $1s0d$ shell space predict a very strong transition in this nucleus at 10.62 MeV, no such transition was found in the region $6.5 < E_x < 15$ MeV. However, the sum of the fragmented $M1$ transition strength observed was somewhat higher than the shell-model value.

ACKNOWLEDGMENTS

The authors wish to thank the DALINAC accelerator staff and associates for their invaluable help in acquiring the data. This work was supported in part by the National Science Foundations under Grants PHY-8519381 and PHY-8820654 (experiment) and PHY-90-17077 (theory), and by the German Federal Ministry for Research and Technology (BMFT) under Contract No. 06DA641I.

[1] A. Johnston and T. E. Drake, J. Phys. A **7**, 898 (1974).
[2] R. Schneider, A. Richter, A. Schwierczinski, E. Spamer, and O. Titze, Nucl. Phys. **A323**, 13 (1979).
[3] C. Rangacharyulu, E. J. Ansaldo, D. Stockhausen, D. Bender, S. Müller, A. Richter, N. Loludice, and F. Palumbo, Phys. Rev. C **31**, 1656 (1985).
[4] S. Raman, L. W. Fagg, and R. S. Hicks, in *Electric and Magnetic Giant Resonances in Nuclei*, edited by J. Speth (World Scientific, Singapore, 1991).
[5] U. E. P. Berg, K. Wienhard, and H. Wolf, Phys. Rev. C **11**, 1851 (1975).
[6] U. E. P. Berg and K. Wienhard, Nucl. Phys. **A318**, 453 (1979).
[7] U. E. P. Berg and U. Kneissl, Annu. Rev. Nucl. Part. Sci. **37**, 33 (1987).
[8] P. E. Burt, L. W. Fagg, H. Crannell, D. I. Sober, W. Stapor, J. T. O'Brien, J. W. Lightbody, X. K. Maruyama, R. A. Lindgren, and C. P. Sargent, Phys. Rev. C **29**, 713 (1984).
[9] L. W. Fagg, W. L. Bendel, E. C. Jones, L. Cohen, and H. F. Kaiser, Phys. Rev. C **5**, 120 (1972).
[10] B. A. Brown and B. H. Wildenthal, Nucl. Phys. **A474**, 290 (1987).
[11] I. S. Towner and F. C. Khanna, Nucl. Phys. **A399**, 334 (1983).
[12] A. Arima, K. Shimizu, W. Bentz, and H. Hyuga, Adv. Nucl. Phys. **18**, 1 (1986).
[13] A. Richter, A. Weiss, O. Häusser, and B. A. Brown, Phys. Rev. Lett. **65**, 2519 (1990).
[14] C. W. Foltz, Ph.D. dissertation, The Catholic University of America, 1991.
[15] H.-D. Gräf, H. Miska, E. Spamer, O. Titze, and Th. Walcher, Nucl. Instrum. Methods **153**, 9 (1978).
[16] D. Bender, Ph.D. dissertation, Technische Hochschule Darmstadt, 1982.
[17] C. Rangacharyulu, E. J. Ansaldo, D. Bender, A. Richter, and E. Spamer, Nucl. Phys. **A406**, 493 (1983).
[18] L. W. Fagg, E. C. Jones, Jr., and W. L. Bendel, Nucl. Instrum. Methods **17**, 136 (1970).
[19] Th. Walcher, R. Frey, H.-D. Gräf, E. Spamer, and H. Theisen, Nucl. Instrum. Methods **153**, 17 (1978).
[20] D. Schüll, J. Foh, H.-D. Gräf, H. Miska, R. Schneider, E. Spamer, H. Theissen, O. Titze, and Th. Walcher, Nucl. Instrum. Methods **153**, 29 (1978).
[21] J. Bergstrom, Univ. of Saskatchewan report, 1974 (unpublished).
[22] J. M. Finn, Hall Crannell, P. L. Hallowell, J. T. O'Brien, and S. Penner, Nucl. Phys. **A274**, 28 (1976).
[23] H. Theissen, Springer Tracts Mod. Phys. **65**, 1 (1972).
[24] B. A. Brown, computer code DENS.
[25] M. Rosen, R. Raphael, and H. Überall, Phys. Rev. **163**, 927 (1967).
[26] P. M. Endt, Nucl. Phys. **A521**, 1 (1990).
[27] B. A. Brown and B. H. Wildenthal, Annu. Rev. Nucl. Part. Sci. **38**, 29 (1988).
[28] B. H. Wildenthal, in *Progress in Particle and Nuclear Physics*, edited by D. H. Wilkenson (Pergamon, Oxford, 1984), Vol. 11, p. 5.
[29] M. C. Etchegoyen, A. Etchegoyen, B. H. Wildenthal, B. A. Brown, and J. Keinonen, Phys. Rev. C **38**, 1382 (1988).
[30] D. I. Sober, B. C. Metsch, W. Knüpfer, G. Eulenberg, G. Küchler, A. Richter, E. Spamer, and W. Steffen, Phys. Rev. C **31**, 2054 (1985). The factor 9/28 in the equation following Eq. (10) is derived for $f_{7/2} \rightarrow f_{5/2}$ transitions, and is replaced by 9/20 for $d_{5/2} \rightarrow d_{3/2}$ transitions in the present work.
[31] D. Kurath, Phys. Rev. **130**, 1525 (1963).

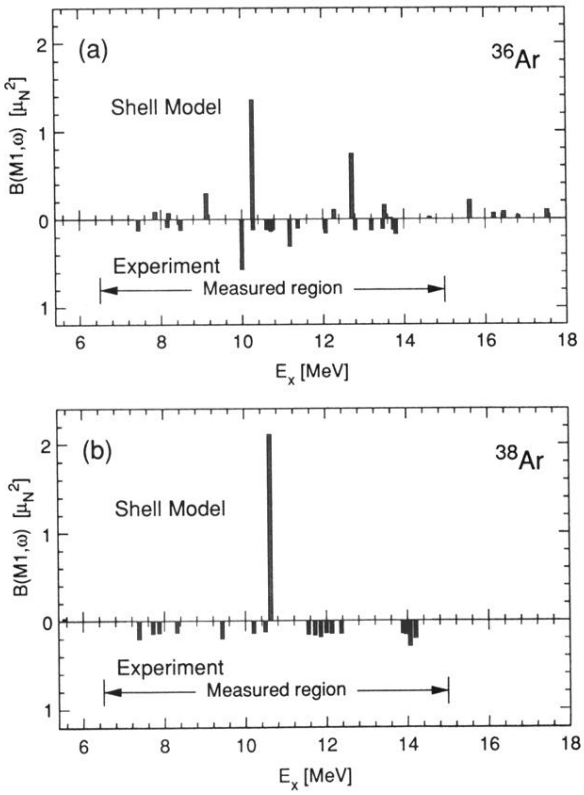

FIG. 7. (a) Theoretical and experimental $M1$ strength in ^{36}Ar. The shell-model calculations are the $1s0d$-shell calculations described in the text, using the effective $M1$ operator. (b) Theoretical and experimental $M1$ strength in ^{38}Ar.